The Astrophysical Journal Letters, 869:L5 (6pp), 2018 December 10 https://doi.org/10.3847/2041-8213/aaf19e

Compressed Magnetic Field in the Magnetically Regulated Global Collapsing Clump of G9.62+0.19

Tie Liu[1,2], Kee-Tae Kim[1], Sheng-Yuan Liu[3], Mika Juvela[4], Qizhou Zhang[5], Yuefang Wu[6], Pak Shing Li[7], Harriet Parsons[2], Archana Soam[1,8], Paul F. Goldsmith[9], Yu-Nung Su[3], Ken'ichi Tatematsu[10], Sheng-Li Qin[11], Guido Garay[12], Tomoya Hirota[10], Jan Wouterloot[2], Huei-Ru Chen[13], Neal J. Evans II[1,14], Sarah Graves[2], Sung-ju Kang[1], Di Li[15,16], Diego Mardones[12,17], Mark G. Rawlings[2], Zhiyuan Ren[15], and Ke Wang[18,19]

[1] Korea Astronomy and Space Science Institute 776, Daedeokdae-ro, Yuseong-gu, Daejeon, 34055, Republic of Korea; liutiepku@gmail.com
[2] East Asian Observatory, 660 North A'ohoku Place, Hilo, HI 96720, USA
[3] Academia Sinica, Institute of Astronomy and Astrophysics, P.O. Box 23-141, Taipei 106, Taiwan
[4] Department of Physics, P.O. Box 64, FI-00014, University of Helsinki, Finland
[5] Harvard-Smithsonian Center for Astrophysics, 60 Garden Street, Cambridge, MA 02138, USA
[6] Department of Astronomy, Peking University, Beijing 100871, People's Republic of China
[7] Astronomy Department, University of California, Berkeley, CA 94720, USA
[8] SOFIA Science Center, USRA, NASA Ames Research Center, N232 Moffett Field, CA 94035, USA
[9] Jet Propulsion Laboratory, California Institute of Technology, 4800 Oak Grove Drive, Pasadena, CA 91109, USA
[10] National Astronomical Observatory of Japan, 2-21-1 Osawa, Mitaka, Tokyo 181-8588, Japan
[11] Department of Astronomy, Yunnan University, and Key Laboratory of Astroparticle Physics of Yunnan Province, Kunming, 650091, People's Republic of China
[12] Departamento de Astronomía, Universidad de Chile, Casilla 36-D, Santiago, Chile
[13] Institute of Astronomy and Department of Physics, National Tsing Hua University, Hsinchu, Taiwan
[14] Department of Astronomy, The University of Texas at Austin, 2515 Speedway, Stop C1400, Austin, TX 78712-1205, USA
[15] University of Chinese Academy of Sciences, Beijing 100049, People's Republic of China
[16] Key Laboratory for Radio Astronomy, Chinese Academy of Sciences, Nanjing 210008, People's Republic of China
[17] Centre for Astrochemical Studies, Max-Planck-Institute for Extraterrestrial Physics, Giessenbachstrasse 1, 85748, Garching, Germany
[18] Kavli Institute for Astronomy and Astrophysics, Peking University, 5 Yiheyuan Road, Haidian District, Beijing 100871, People's Republic of China
[19] European Southern Observatory (ESO) Headquarters, Karl-Schwarzschild-Str. 2, 85748 Garching bei München, Germany
Received 2018 September 25; revised 2018 November 11; accepted 2018 November 16; published 2018 December 4

Abstract

How stellar feedback from high-mass stars (e.g., H II regions) influences the surrounding interstellar medium and regulates new star formation is still unclear. To address this question, we observed the G9.62+0.19 complex in 850 μm continuum with the James Clerk Maxwell Telescope/POL-2 polarimeter. An ordered magnetic field has been discovered in its youngest clump, the G9.62 clump. The magnetic field strength is determined to be ~1 mG. Magnetic field plays a larger role than turbulence in supporting the clump. However, the G9.62 clump is still unstable against gravitational collapse even if thermal, turbulent, and magnetic field support are taken into account together. The magnetic field segments in the outskirts of the G9.62 clump seem to point toward the clump center, resembling a dragged-in morphology, indicating that the clump is likely undergoing magnetically regulated global collapse. However, the magnetic field in its central region is aligned with the shells of the photodissociation regions and is approximately parallel to the ionization (or shock) front, indicating that the magnetic field therein is likely compressed by the expanding H II regions that formed in the same complex.

Key words: ISM: magnetic fields

1. Introduction

Stellar feedback from massive stars can exert a strong influence on the surrounding medium and regulate the subsequent star formation (Elmegreen & Lada 1977; Whitworth et al. 1994a, 1994b). The presence of feedback-influenced star formation process has been suggested in the borders of several H II regions as evidenced by fragmented shells, the age sequence of stars, or the overdensity of young stellar objects (Zavagno et al. 2006, 2007; Liu et al. 2012, 2015, 2016; Thompson et al. 2012). However, it is still unclear how stellar feedback from high-mass stars (e.g., H II regions) influences the surrounding interstellar medium and regulates new star formation.

Magnetohydrodynamic (MHD) simulations demonstrated that the global magnetic field lines may roughly trace the outline of the expanding shell from a young massive star and are parallel to the long axis of the adjacent compressed filament (e.g., Klassen et al. 2017). This is strong evidence for stellar feedback. Recent near-infrared polarization observations have found that the magnetic field in the shells near H II regions or infrared bubbles is curved and follows the shells, and the magnetic field strength in the shells is significantly enhanced compared to the ambient field strength (e.g., Chen et al. 2017). These near-infrared polarization observations are consistent with the simulations but only trace low-density, diffuse cloud material due to high dust extinction in the densest part of the shells.

In contrast to near-infrared polarization observations, polarized submillimeter thermal dust emission can trace magnetic field in dense regions of clouds (Hull et al. 2013; Zhang et al. 2014). To this end, we observed the G9.62+0.19 complex in 850 μm polarized continuum with the POL-2 polarimeter (Friberg et al. 2016) in conjunction with Submillimetre Common-User Bolometer Array 2 (SCUBA-2; Holland et al. 2013) at the 15 m James Clerk Maxwell Telescope (JCMT) telescope. Located at a distance of 5.2 kpc (Sanna et al. 2009), the G9.62+0.19 complex is an active high-mass star-forming region. Sequential high-mass star formation (from high-mass starless cores, hot molecular cores, UC H II regions

to expanding H II regions) is taking place in this region (Hofner et al. 1994, 1996, 2001; Testi et al. 2000; Liu et al. 2011, 2017). Therefore, the G9.62+0.19 complex is an ideal target to study the effect of stellar feedback from expanding H II regions on next generations of high-mass star formation. Liu et al. (2017) suggested that the youngest star-forming clump in this region (i.e., the G9.62 clump) is gravitationally unstable and will further collapse if only turbulent support is considered.

In this Letter, we discuss the magnetic field geometry as well as magnetic field strength in the G.62 clump. In particular, we investigate how the magnetic field responds to stellar feedback and regulates the star formation in the G9.62 clump.

2. Observations

The POL-2 observations of the G9.62 clump (project code: M18BP019; PI: T. Liu) were conducted in 2018 August using the POL-2 DAISY mapping mode (Holland et al. 2013; Friberg et al. 2016). The total integration time was 1.8 hr under JCMT Band 2 weather condition, with the atmospheric optical depth at 225 GHz of $0.05 < \tau_{225} < 0.08$. The observing strategy is the same as described by Ward-Thompson et al. (2017). Data reduction is performed using a python script called *pol2map* written within the STARLINK/SMURF package (Chapin et al. 2013; Currie et al. 2014), which is specific for submillimeter data reduction (much of it is specific to the JCMT). The output polarization percentage values are debiased using the mean of their Q and U variances to remove statistical biasing in regions of low signal-to-noise. The details of data reduction with *pol2map* can be found in some previous POL-2 papers (Kwon et al. 2018; Liu et al. 2018; Pattle et al. 2018; Soam et al. 2018). Our method slightly differs from those previous works by utilizing the new *skyloop*[20] parameter in *pol2map* and the correction of synchronization loss between data values and pointing information in the data reduction process, which improve the ability to recover faint extended structures. The final co-added maps have rms noise levels of ∼4 mJy/beam for a beam size of 14.″1. Throughout this Letter, polarization angles are measured from the North increasing toward the East, following the IAU convention. The polarization orientations obtained are rotated by 90° to infer the magnetic field orientations projected on the plane of sky.

Planck 850 μm (353 GHz) data are used to examine the dust emission and the dust polarization at scales larger than 5′ (Juvela et al. 2018).

3. Results

3.1. Orientations of Magnetic Field

Panel (a) of Figure 1 shows the magnetic field morphology observed by Planck. The magnetic field orientations in the Planck data are quite uniform with a mean angle of ∼42° and a small angle dispersion of ∼4°. The field direction is well aligned with the large-scale (∼100 pc) Galactic field direction. As shown in panel (b) of Figure 1, four smaller clumps separated by ∼5 pc were detected in the POL-2 observations. Interestingly, the four clumps are aligned along a line that is roughly perpendicular to the large-scale magnetic field revealed by Planck, indicating that magnetic field may play an important role in the formation and fragmentation process of molecular clumps at the pc scale.

[20] http://starlink.eao.hawaii.edu/docs/sun258.htx/sun258ss72.html

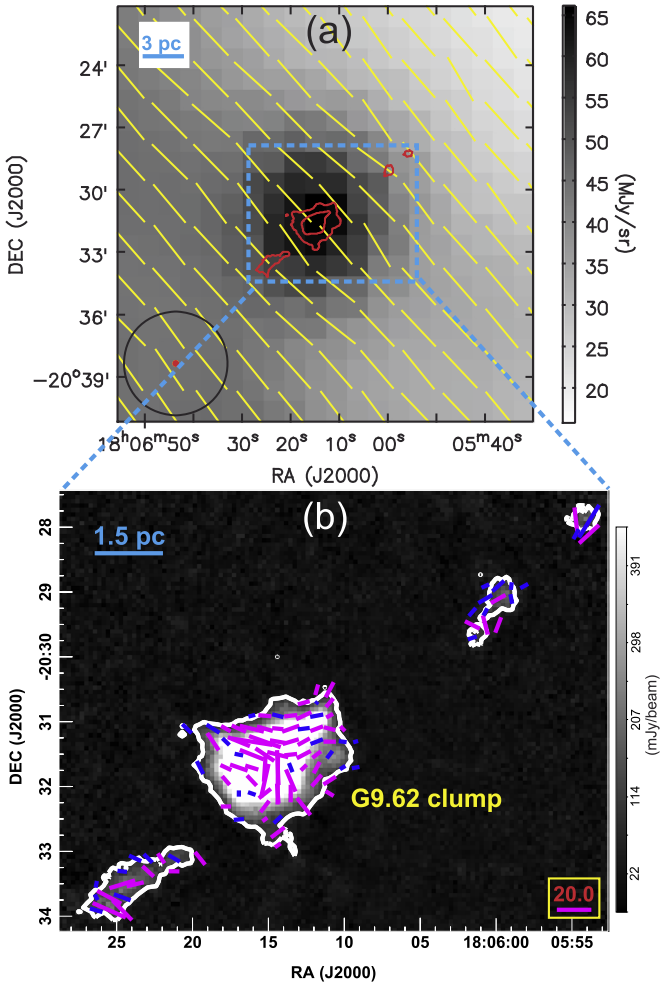

Figure 1. (a) Planck 353 GHz magnetic field segments overlaid on the 353 GHz continuum emission shown in grayscale. The contours show the JCMT/POL-2 850 μm Stokes I intensity map. The contour levels are 50 and 500 mJy beam^{-1}. The beams of Planck (black circle) and JCMT (filled red circle) are shown in the lower-left corner. (b) JCMT/POL-2 magnetic field segments overlaid on the Stokes I intensity map at 850 μm. The contour is at 50 mJy beam^{-1}. The segments with Stokes I intensity $I/\delta I > 10$ are shown with a pixel size of 12″. The length of segments represents their polarized intensity in units of mJy beam^{-1}. The magenta segments have polarization fraction $P/\delta P > 3$, while the blue segments have $2 < P/\delta P < 3$.

The magnetic field within the clumps as revealed by POL-2 shows a more complex behavior, with no preferred orientation. Although complexity is observed when considering the region as a whole, the field becomes more structured in the G9.62 clump as shown in panel (a) of Figure 2. We have identified six magnetic field components with underlying uniform field geometry. The neighboring magnetic field segments with angle differences smaller than ∼15° from each other are assigned to the same component. These components are clearly separated from each other with the mean angles differing by $\gtrsim$40°. They have small angle dispersions ($\lesssim$16°), suggesting that the magnetic field is quite uniform within individual sub-regions of the G9.62 clump. They are color coded in panel (a) of Figure 2. The statistics of those magnetic field components are shown in Table 1. The "JCMT-yellow" component shows similar orientations (∼58°) as the large-scale magnetic field revealed by Planck. The other components, however, show much larger deviation (>50°) from the large-scale magnetic field.

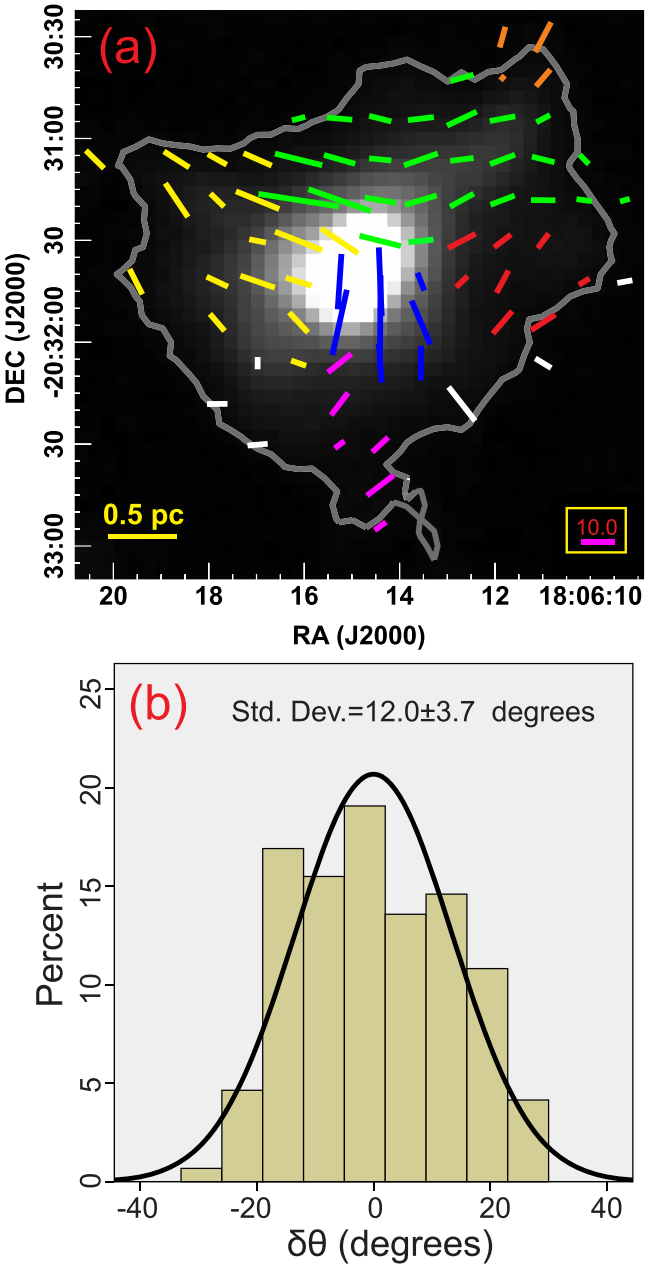

Figure 2. (a) JCMT/POL-2 magnetic field segments overlaid on Stokes I intensity map at 850 μm in the G9.62 clump. The contour is at 50 mJy beam^{-1}. The segments with polarization fraction $P/\delta P > 2$ are shown with a pixel size of 12″. The different magnetic field components with underlying uniform field geometry are color coded. The segments in white are not included in the analysis. (b) The distribution of the residual angles ($\delta\theta$) with $P/\delta P > 2$. The distribution is weighted by $P/\delta P$.

3.2. Magnetic Field Strength

We estimated the plane-of-sky magnetic field strength ($B_{\rm pos}$) for the G9.62 clump using the Davis–Chandrasekhar–Fermi (DCF) method (Davis 1951; Chandrasekhar & Fermi 1953):

$$B_{\rm pos} = Q'\sqrt{4\pi\rho}\,\frac{\sigma_{\rm NT}}{\sigma_\theta} \approx 9.3\sqrt{\frac{n({\rm H_2})}{({\rm cm^{-3}})}}\,\frac{\Delta v/({\rm km\ s^{-1}})}{\sigma_\theta/({\rm degrees})}\,\mu{\rm G}, \quad (1)$$

where Q' is a factor of order unity accounting for variations in field strength on scales smaller than the beam (Crutcher et al. 2004), $\rho = \mu_g m_{\rm H} n_{\rm H_2}$ is the gas density. Here Q' is taken as 0.5

Table 1
Statistics of the Orientations of Magnetic Field Segments

Component[a]	Number	Min. (°)	Max. (°)	Mean[b] (°)	σ_θ[b] (°)
Planck	930	25.1	67.7	41.6	4.0
JCMT-all	110	2.4	180.0	91.1	44.8
JCMT-red	8	117.7	151.5	130.7	11.0
JCMT-blue	7	−12.5[c]	23.2	1.3	11.4
JCMT-yellow	17	26.8	78.7	58.2	13.1
JCMT-green	26	70.6	119.1	93.0	16.1
JCMT-orange	4	139.4	164.6	149.2	10.8
JCMT-magenta	6	125.7	143.0	130.8	6.4

Notes.
[a] Planck: Planck 353 GHz magnetic field segments within 30′ × 30′ region; JCMT-all: JCMT/POL-2 magnetic field segments of the three clumps within the 50 mJy beam^{-1} contours of Stokes I intensity in panel (b) of Figure 1. The "JCMT-color" components correspond to the segments with different colors in panel (a) of Figure 2.
[b] The statistics of angles with $P/\delta P > 2$. The mean angle and angle dispersion (σ_θ) are weighted by $P/\delta P$.
[c] The negative value is caused by the 180° ambiguity in magnetic field direction. A value of −180° is added to the segments with angles >90°.

(Ostriker et al. 2001). We adopt the clump-averaged number density of $n_{\rm H_2} = (9.1 \pm 0.7) \times 10^4$ cm^{-3} (Liu et al. 2017). Δv is the FWHM velocity dispersion ($\sim 3.4 \pm 0.1$ km s^{-1}) derived from the C^{18}O (3–2) line observed with the JCMT (Liu et al. 2017). σ_θ is the dispersion in polarization position angles.

We subtract a mean angle from the measured position angles in each magnetic field component, giving residual angles ($\delta\theta$) showing the deviation in angle from the mean field direction. The distribution of the residual angles ($\delta\theta$) of the six magnetic field components is shown in panel (b) of Figure 2. The dispersion in polarization position angle (σ_θ) estimated from this distribution is $\sim 13\overset{\circ}{.}4 \pm 3\overset{\circ}{.}7$. After correcting the angular dispersion for mean angle measurement uncertainty ($\sim 6\overset{\circ}{.}1$), the σ_θ becomes $\sqrt{13.4^2 - 6.1^2} \approx 12\overset{\circ}{.}0$. Because of significant changes in magnetic field orientations among different magnetic field components and the limited pixel numbers, we did not apply other methods (like the "unsharp masking method" Pattle et al. 2017) to remove the underlying uniform magnetic field. Without the exact knowledge of the uniform field, the derived σ_θ is not very precise. However, the σ_θ, is smaller than the maximum value at which the standard DCF method can be safely applied ($\leqslant 25°$; Heitsch et al. 2001). Therefore, the derived σ_θ could be representative of the real angular dispersion, allowing us to perform an order-of-magnitude estimation of magnetic field strength and energies in the G9.62 clump.

The estimated $B_{\rm pos}$ is $\sim 790 \pm 190$ μG. Hereafter, the errors for derived parameters (e.g., $B_{\rm pos}$) are estimated using standard error propagation. The magnetic field strength is significantly larger than that observed in some infrared dark clouds (e.g., ~ 270 μG in G11.11–0.12; ~ 100 μG in G035.39–00.33; Pillai et al. 2015; Liu et al. 2018) on similar spatial scales. Statistically, the total magnetic field strength is 1.3 times $B_{\rm pos}$ considering projection effects (Crutcher et al. 2004). Applying the same correction factor, the total magnetic field strength ($B_{\rm tot}$) in the G9.62 clump is $\sim 1030 \pm 250$ μG. We should note that the correction factor was derived from statistical studies and may not apply precisely to any individual region.

The corresponding Alfvénic velocity is

$$\sigma_{\rm A} = \frac{B_{\rm tot}}{\sqrt{4\pi\rho}}. \quad (2)$$

The derived $\sigma_{\rm A}$ is $\sim 4.5 \pm 1.2\,{\rm km\,s^{-1}}$. The Alfvén Mach number is

$$\mathcal{M}_{\rm A} = \sqrt{3}\,\sigma_{\rm NT}/\sigma_{\rm A} \quad (3)$$

where $\sigma_{\rm NT} \sim 1.5\,{\rm km\,s^{-1}}$ is the mean nonthermal velocity dispersion derived from $C^{18}O$ (3–2) line (Liu et al. 2017). $\mathcal{M}_{\rm A}$ is $\sim 0.6 \pm 0.2$, suggesting that the turbulent motions are sub-Alfvénic in the G9.62 clump.

4. Discussions

4.1. Gravitational Stability of the G9.62 Clump

Liu et al. (2017) suggested that the G9.62 clump is gravitationally unstable if only turbulent support is considered. Therefore, the question we wish to ask is: does the magnetic field play a role in supporting the G9.62 clump?

To investigate the gravitational stability of the G9.62 clump, we estimated its virial mass ($M^B_{\rm vir}$) considering thermal, turbulent, and magnetic pressure (Bertoldi & McKee 1992; Hennebelle & Chabrier 2008; Pillai et al. 2011):

$$M^B_{\rm vir} = 3\frac{R_{\rm eff}}{G}\left(\frac{5-2n}{3-n}\right)\left(\sigma^2_{\rm NT} + C_s^2 + \frac{\sigma^2_{\rm A}}{6}\right) \quad (4)$$

where n is the power-law index for a density profile, $\rho(r)$, as a function of the distance (r) from the clump center, $\rho(r) \propto r^{-n}$. Mueller et al. (2002) derived a power-law index $n \sim 2$ for the G9.62 clump. $R_{\rm eff}$ of 0.5 pc is the effective radius of the clump estimated from the SCUBA-2 850 μm continuum data (Liu et al. 2017). The 1D thermal velocity dispersion (or sound speed C_s) is $0.35\,{\rm km\,s^{-1}}$ for a temperature of 35 K (Liu et al. 2017). For a $\sigma_{\rm A}$ of $\sim 4.5\,{\rm km\,s^{-1}}$ and a $\sigma_{\rm NT}$ of $\sim 1.5\,{\rm km\,s^{-1}}$, the virial mass is $\sim 1900 \pm 600\,M_\odot$, which is smaller than the clump mass $\sim 2800 \pm 200\,M_\odot$ (Liu et al. 2017), indicating that the G9.62 clump is unstable against gravitational collapse even if thermal, turbulent, and magnetic field support are taken into account together. Magnetic field plays a ($\sim$1.5 times) larger role than turbulence in supporting the clump.

We also notice that most of the magnetic field segments (such as the white, yellow, and orange segments in panel (a) of Figure 2) in the outskirts of the G9.62 clump seem to point toward the clump center, resembling a dragged-in morphology as seen in other magnetically regulated collapsing cores (e.g., Tang et al. 2009; Koch et al. 2018). The magnetic field geometry and the gravitational stability of the G9.62 clump indicate that it may be undergoing magnetically regulated global collapse.

4.2. Compressed Magnetic Field Due to Stellar Feedback from Expanding H II Regions

Although the G9.62 clump seems to be undergoing magnetically regulated global collapse, its magnetic field morphology also indicates influences of stellar feedback from the older generations of expanding H II regions formed in the same complex.

As shown in panel (a) of Figure 2, the magnetic field segments (e.g., JCMT-blue and JCMT-green components) in the central region do not follow a dragged-in (e.g., hour-glass) morphology caused by gravitational collapse. In panel (a) of Figure 3, we take a closer look at the magnetic field segments in its central region. The dense filament as revealed by the ALMA 1.3 mm continuum (shown as color image in the panel (a) of Figure 3) has a position angle of $\sim 162°$. The magnetic field segments are roughly parallel to the dense filament in its southern part, while the magnetic field segments become roughly perpendicular to the dense filament in its northern part. Previous polarization observations of filamentary clouds (Chapman et al. 2011; Cox et al. 2016; Juvela et al. 2018; Liu et al. 2018) found that magnetic field tends to be roughly perpendicular to the longer axes of the dense parts of filaments, indicating that the dense filaments are collapsing along magnetic field or still accreting gas along magnetic field from their surroundings. This is very different from the dense filament in the G9.62 clump. Liu et al. (2017) suggested that the G9.62 clump is compressed by the expanding H II regions ("B" and "C") to its west. Therefore, below we argue that the magnetic field in the G9.62 clump seems to be compressed as the expanding H II regions grow.

The *Spitzer*/IRAC 8 μm emission is mainly dominated by polycyclic aromatic hydrocarbons emission and is a good tracer of photodissociation regions (PDRs; Churchwell et al. 2006). The 8 μm emission in panel (b) of Figure 3 reveals the PDRs of the two expanding H II regions. We gridded the 8 μm data to a 4 arcsec pixel size, the same as POL-2 data, to derive the 8 μm intensity gradients with the function "gradient"[21] in MATLAB. As shown in panel (b) of Figure 3, the magnetic field segments in the outskirts of "B" and "C" roughly follow the 8 μm intensity contours and are perpendicular to the 8 μm intensity gradients. In panel (c) of Figure 3, we investigate the angle differences ($\Delta\theta$) between magnetic field segments and 8 μm intensity gradients as a function of 8 μm intensity ($F_{8\mu\rm m}$) for pixels with $F_{8\mu\rm m} > 100\,{\rm MJy\,sr^{-1}}$. A clear decreasing trend in the $\Delta\theta$ versus $F_{8\mu\rm m}$ relation is found as

$$\frac{\Delta\theta}{(\rm degrees)} = -(18.0 \pm 3.3)\ln\left(\frac{F_{8\mu\rm m}}{({\rm MJy\,sr^{-1}})}\right) + (163.3 \pm 21.2), \quad (5)$$

with the correlation coefficient $R = 0.63$. This is a further indication that the magnetic field surrounding the expanding H II regions follows the outlines of the expanding shells and is approximately parallel to the ionization (or shock) front. In numerical simulations of expanding H II regions, a shell of material is swept up as the H II region grows and the magnetic field inside the shell is approximately parallel to the ionization front (Arthur et al. 2011; Klassen et al. 2017), which is consistent with our findings here.

In numerical simulations, the magnetic field strength is enhanced by a factor of about 5 to 6 in the compressed shell when comparing the magnetic field strength inside the expanding H II regions (Klassen et al. 2017). If we adopt the same enhancement factor, the magnetic field strength inside the expanding H II regions ("B" and "C") should be $\sim 200\,\mu$G. The total magnetic pressure (P_B) is

$$P_B = \frac{B^2_{\rm tot}}{8\pi k_{\rm B}} \quad (6)$$

[21] https://www.mathworks.com/help/matlab/ref/gradient.html

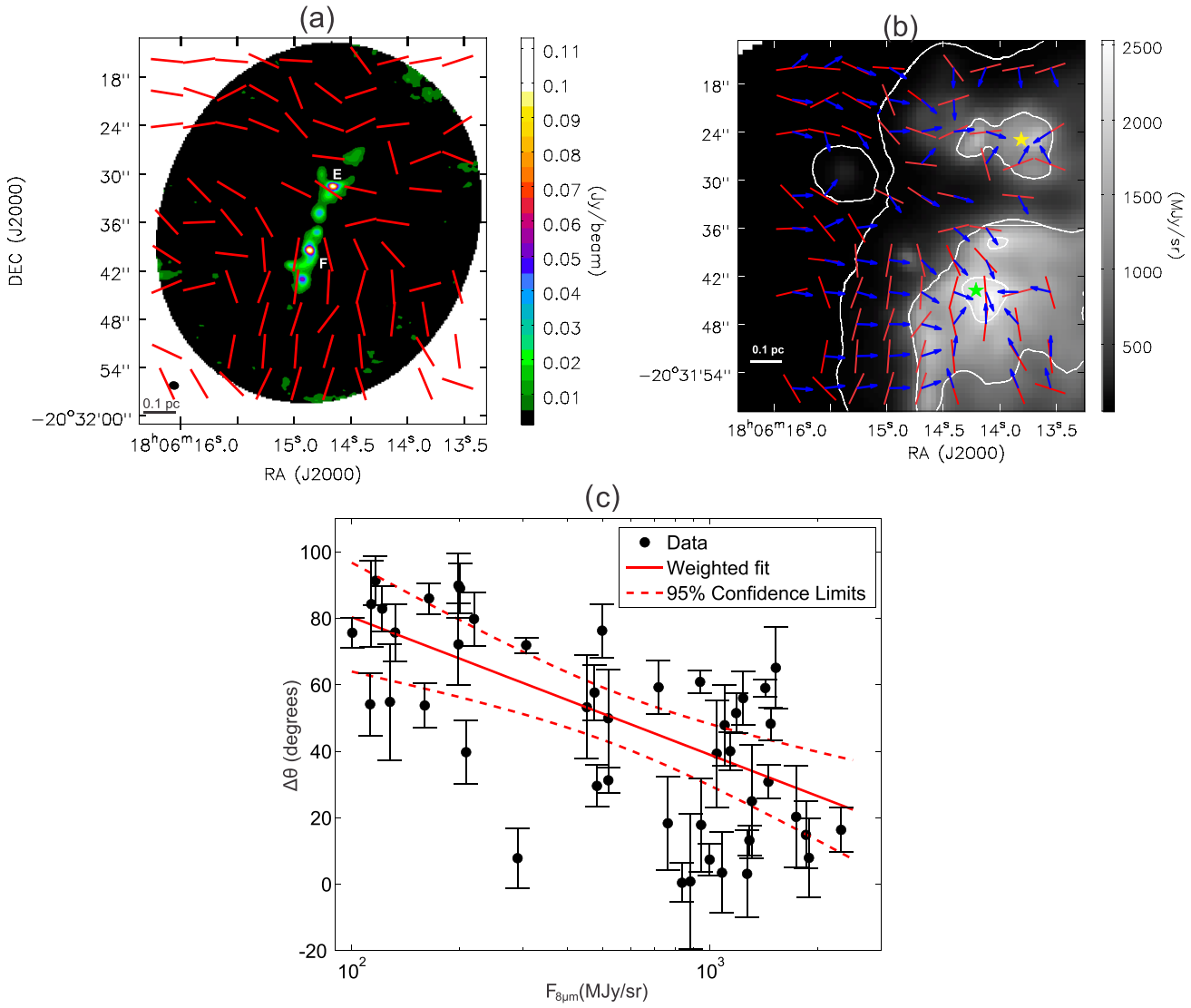

Figure 3. (a) JCMT/POL-2 magnetic field segments overlaid on the ALMA 1.3 mm continuum image (Liu et al. 2017). The pixel size of POL-2 data shown here is 4″. The ALMA beam is shown as the filled circle in the lower-left corner. The two brightest cores in the ALMA image are "E" (the northern one) and "F" (the southern one). (b) JCMT/POL-2 magnetic field segments (red) overlaid the *Spitzer*/IRAC 8 μm emission shown as a gray image and white contours. The contour levels are 100, 1000, and 2000 MJy sr^{-1}. The two expanding H II regions are marked with stars ("B" in green and "C" in yellow). The blue arrows show the directions of *Spitzer*/IRAC 8 μm intensity gradients. (c) The angle differences ($\Delta\theta$) between magnetic field segments and 8 μm intensity gradients as a function of 8 μm intensity ($F_{8\mu m}$). The solid red line is the best fit to the data considering the uncertainties of magnetic field angles. The dashed red lines are the confidence ranges of the best fit.

where k_B is the the Boltzmann constant. The estimated P_B inside the H II regions is $\sim 1 \times 10^7$ K cm^{-3}, which is smaller than the ionized gas pressure ($\sim 4 \times 10^7$ K cm^{-3}) derived by Liu et al. (2017), suggesting that the magnetic field cannot prevent H II regions from further expanding. The magnetic field may also have being compressed as the H II regions expand (Arthur et al. 2011; Klassen et al. 2017).

4.3. Comparison with Core-scale Magnetic Field

Dall'Olio (2017) recently observed the magnetic field at ~336 GHz around dense cores "E" and "F" (the two brightest cores in panel (a) of Figure 3) with ALMA. The magnetic field around "E" roughly follows an east–west direction and is perpendicular to the filament long axis, while the magnetic field around "F" is parallel to the filament. The orientations of the magnetic field segments in the ALMA observations are consistent with those in our JCMT/POL-2 observations. This consistency of clump-scale and core-scale magnetic field orientations may suggest that the fragmentation in the G9.62 clump is regulated by magnetic field.

Liu et al. (2017) found a lack of a widespread low-mass protostellar population and suggested that the core fragmentation or low-mass star formation is suppressed due to feedback from young OB stars in the G9.62 clump by heating the cores up and injecting turbulence through outflows, leading to an increase of the Jeans mass. MHD simulations suggested that the combination of magnetic field and radiation feedback is even more effective at suppressing fragmentation (Myers et al. 2013). The very ordered magnetic field revealed by ALMA around the two bright cores "E" and "F" (Dall'Olio 2017) indicates strong magnetic field strength at the core scale. Therefore, we suggest that core fragmentation in the G9.62 clump is very likely suppressed due to the joint effect of the strong magnetic field and feedback (e.g., radiation, outflows) from young OB stars. Indeed, higher angular resolution (0.″3 or

~1500 au) ALMA observations at 336 GHz indicate that the massive cores in the G9.62 clump are not highly fragmented (Dall'Olio 2017).

The James Clerk Maxwell Telescope is operated by the East Asian Observatory on behalf of The National Astronomical Observatory of Japan; Academia Sinica Institute of Astronomy and Astrophysics; the Korea Astronomy and Space Science Institute; the Operation, Maintenance and Upgrading Fund for Astronomical Telescopes and Facility Instruments, budgeted from the Ministry of Finance (MOF) of China and administrated by the Chinese Academy of Sciences (CAS), as well as the National Key R&D Program of China (No. 2017YFA0402700). Additional funding support is provided by the Science and Technology Facilities Council of the United Kingdom and participating universities in the United Kingdom and Canada. The Starlink software (Currie et al. 2014) used in POL-2 data reduction is currently supported by the East Asian Observatory. Tie Liu is supported by EACOA fellowship. M.J. acknowledges the support of the Academy of Finland grant No. 285769. This Letter was carried out in part at the Jet Propulsion Laboratory, which is operated for NASA by the California Institute of Technology. This Letter is partially supported by the National Key R&D Program of China Nos. 2017YFA0402600, 2017YFA0402702, and NSFC No. 11433008, No. 11725313, and No. 11721303. D.M. acknowledges support from CONICYT project Basal AFB-170002. Ke Wang also acknowledges support by the German Research Foundation (WA3628-1/1).

ORCID iDs

Tie Liu https://orcid.org/0000-0002-5286-2564
Kee-Tae Kim https://orcid.org/0000-0003-2412-7092
Sheng-Yuan Liu https://orcid.org/0000-0003-4603-7119
Mika Juvela https://orcid.org/0000-0002-5809-4834
Qizhou Zhang https://orcid.org/0000-0003-2384-6589
Yuefang Wu https://orcid.org/0000-0002-5076-7520
Harriet Parsons https://orcid.org/0000-0002-6327-3423
Archana Soam https://orcid.org/0000-0002-6386-2906
Paul F. Goldsmith https://orcid.org/0000-0002-6622-8396
Ken'ichi Tatematsu https://orcid.org/0000-0002-8149-8546
Sheng-Li Qin https://orcid.org/0000-0003-2302-0613
Tomoya Hirota https://orcid.org/0000-0003-1659-095X
Huei-Ru Chen https://orcid.org/0000-0002-9774-1846
Sarah Graves https://orcid.org/0000-0001-9361-5781
Sung-ju Kang https://orcid.org/0000-0002-5004-7216
Diego Mardones https://orcid.org/0000-0002-5065-9175
Ke Wang https://orcid.org/0000-0002-7237-3856

References

Arthur, S. J., Henney, W. J., Mellema, G., et al. 2011, MNRAS, 414, 1747
Bertoldi, F., & McKee, C. F. 1992, ApJ, 395, 140
Chandrasekhar, S., & Fermi, E. 1953, ApJ, 118, 116
Chapin, E. L., Berry, D. S., Gibb, A. G., et al. 2013, MNRAS, 430, 2545
Chapman, N. L., Goldsmith, P. F., Pineda, J. L., et al. 2011, ApJ, 741, 21
Chen, Z., Jiang, Z., Tamura, M., et al. 2017, ApJ, 838, 80
Churchwell, E., Povich, M. S., Allen, D., et al. 2006, ApJ, 649, 759
Cox, N. L. J., Arzoumanian, D., & André, Ph. 2016, A&A, 590, 110
Crutcher, R. M., Nutter, D. J., Ward-Thompson, D., et al. 2004, ApJ, 600, 279
Currie, M. J., Berry, D. S., Jenness, T., et al. 2014, in ASP Conf. Ser. 485, Astronomical Data Analysis Software and Systems XXIII, ed. N. Manset & P. Forshay (San Francisco, CA: ASP), 391
Dall'Olio, D. 2017, in IV Workshop Sull'Astronomia Millimetrica in Italia, 36, https://indico.ira.inaf.it/event/3
Davis, L. 1951, PhRv, 81, 890
Elmegreen, B. G., & Lada, C. J. 1977, ApJ, 214, 725
Friberg, P., Bastien, P., Berry, D., et al. 2016, Proc. SPIE, 9914, 991403
Heitsch, F., Zweibel, E. G., Mac Low, M.-M., et al. 2001, ApJ, 561, 800
Hennebelle, P., & Chabrier, G. 2008, ApJ, 684, 395
Hofner, P., Kurtz, S., Churchwell, E., et al. 1994, ApJL, 429, L85
Hofner, P., Kurtz, S., Churchwell, E., et al. 1996, ApJ, 460, 359
Hofner, P., Wiesemeyer, H., & Henning, T. 2001, ApJ, 549, 425
Holland, W. S., Bintley, D., Chapin, E. L., et al. 2013, MNRAS, 430, 2513
Hull, C. L. H., Plambeck, R. L., & Bolatto, A. D. 2013, ApJ, 768, 159
Juvela, M., Guillet, V., Liu, T., et al. 2018, A&A, 620, A26
Klassen, M., Pudritz, R. E., & Kirk, H. 2017, MNRAS, 465, 2254
Koch, P. M., Tang, Y.-W., Ho, P. T. P., et al. 2018, ApJ, 855, 39
Kwon, J., Doi, Y., Tamura, M., et al. 2018, ApJ, 859, 4
Liu, H.-L., Li, J.-Z., Wu, Y., et al. 2016, ApJ, 818, 95
Liu, H.-L., Wu, Y., Li, J., et al. 2015, ApJ, 798, 30
Liu, T., Lacy, J., Li, P. S., et al. 2017, ApJ, 849, 25
Liu, T., Li, P. S., Juvela, M., et al. 2018, ApJ, 859, 151
Liu, T., Wu, Y., Liu, S.-Y., et al. 2011, ApJ, 730, 102
Liu, T., Wu, Y., Zhang, H., & Qin, S.-L. 2012, ApJ, 751, 68
Mueller, K. E., Shirley, Y. L., Evans, N. J., II, et al. 2002, ApJS, 143, 469
Myers, A. T., McKee, C. F., Cunningham, A. J., et al. 2013, ApJ, 766, 97
Ostriker, E. C., Stone, J. M., & Gammie, C. F. 2001, ApJ, 546, 980
Pattle, K., Ward-Thompson, D., Berry, D., et al. 2017, ApJ, 846, 122
Pattle, K., Ward-Thompson, D., Hasegawa, T., et al. 2018, ApJ, 860L, 6
Pillai, T., Kauffmann, J., Tan, J. C., et al. 2015, ApJ, 799, 74
Pillai, T., Kauffmann, J., Wyrowski, F., et al. 2011, A&A, 530, A118
Sanna, A., Reid, M. J., Moscadelli, L., et al. 2009, ApJ, 706, 464
Soam, A., Pattle, K., Ward-Thompson, D., et al. 2018, ApJ, 861, 65
Tang, Y.-W., Ho, P. T. P., Koch, P. M., et al. 2009, ApJ, 700, 251
Testi, L., Hofner, P., Kurtz, S., & Rupen, M. 2000, A&A, 359, L5
Thompson, M. A., Urquhart, J. S., Moore, T. J. T., et al. 2012, MNRAS, 421, 408
Ward-Thompson, D., Pattle, K., Bastien, P., et al. 2017, ApJ, 842, 66
Whitworth, A. P., Bhattal, A. S., Chapman, S. J., et al. 1994a, A&A, 290, 421
Whitworth, A. P., Bhattal, A. S., Chapman, S. J., et al. 1994b, MNRAS, 268, 291
Zavagno, A., Deharveng, L., Comerón, F., et al. 2006, A&A, 446, 171
Zavagno, A., Pomarès, M., Deharveng, L., et al. 2007, A&A, 472, 835
Zhang, Q., Qiu, K., Girart, J. M., et al. 2014, ApJ, 792, 116